ELSEVIER

Nuclear Physics A687 (2001) 253c–261c

NUCLEAR PHYSICS A

www.elsevier.nl/locate/npe

Description of single- and multiple-phonon giant dipole resonances within the phonon damping model

Nguyen Dinh Dang[a]

[a]RI-beam factory project office, RIKEN
2-1 Hirosawa, Wako, 351-0198 Saitama, Japan

The phonon damping model is applied to describe: 1) the giant dipole resonance (GDR) in hot nuclei, 2) multiple-phonon resonances, and 3) GDR in neutron-rich nuclei. The results obtained are compared with the recent experimental data and predictions given by other theories.

1. INTRODUCTION

It has been now well established that the width of the giant dipole resonance (GDR) in highly excited (hot) nuclei increases sharply with increasing excitation energy E^* up to $E^* \sim 130$ MeV in tin isotopes [1], and saturates at higher E^* [2]. At $E^* > 300$ MeV a saturation of the integrated yield of γ rays has been observed in regions of the GDR and above it [2,3]. A theoretical model for hot GDR is adequate if it can describe correctly not only the temperature dependence of the width, but also the shape of the GDR as a function of excitation energy E^* (or temperature T).

For the double GDR (DGDR), the experimentally extracted cross section of the Coulomb excitation is significantly larger (by $\sim 33 - 78\%$) than that given by the harmonic picture, in which an n-phonon resonance is built from n non-interacting single-phonon resonances [4]. Anharmonicities so far lead to rather small shifts of the DGDR energy and width from the values predicted by the harmonic picture.

In neutron-rich nuclei, the neutron excess leads to the appearance of the pigmy GDR. So far, the strength distributions of pigmy GDR were just smeared out by a Lorentzian with a finite width, leaving the question of the effect of GDR damping on the strength of the pigmy resonances open.

The phonon damping model (PDM) was proposed by Dinh Dang and Arima in 1997 (the PDM-1) [5] primarily to describe the damping of the hot GDR. It applies the double-time Green's function method to derive the equations for the propagation of the GDR phonon, which is damped due to the presence of a polarization operator containing the effects of coupling to all ph, pp, and hh configurations. The damping of the GDR is defined as the imaginary part of the analytic continuation of the polarization operator in the complex energy plane. The second approximation scheme (PDM-2), proposed by Dinh Dang, Tanabe, and Arima [6], is a further development to include explicitly all the forward-going processes up to two-phonon ones at $T \neq 0$ in the same order of the interaction strength. In the PDM the mechanism that causes the sharp increase of the

0375-9474/01/$ – see front matter
PII S0375-9474(01)00629-7

GDR width at low temperatures, $T \leq 3$ MeV, and its saturation at high temperatures, $T > 3$ - 4 MeV, is coupling of the GDR phonon to the particle-particle (pp) and hole-hole (hh) configurations, which appear due to the deformation of the Fermi surface at $T \neq 0$. In this work, the results of application of PDM in the description of hot GDR, double-, triple-GDRs (DGDR and TGDR), and GDR in neutron rich nuclei are discussed. The results for hot GDR and DGDR are compared with the recent experimental data and those given by other theories.

2. FORMALISM

The model Hamiltonian of the PDM is composed of three terms

$$H = \sum_s E_s a_s^\dagger a_s + \sum_q \omega_q Q_q^\dagger Q_q + \sum_{ss'q} F_{ss'}^{(q)} a_s^\dagger a_{s'} (Q_q^\dagger + Q_q). \tag{1}$$

The first term is the single-particle field, where $a_s^\dagger$ and a_s are creation and destruction operators of a particle (p) or hole (h) state with energy $E_s = \epsilon_s - \epsilon_F$ (ϵ_s is the single-particle energy and ϵ_F is the Fermi energy). The second term is the phonon field with $Q_q^\dagger$ and Q_q being the creation and destruction operators of a phonon with energy ω_q. The last term is the coupling between the first two terms.

2.1. Equations for the damping of hot GDR

The Green's function for the propagation of n-phonon state is derived as [7]:

$$G_{q_1 \ldots q_n}(E) = \frac{n!}{2\pi} \frac{1 + \sum_{i=1}^n \nu_{q_i}}{E - \sum_{i=1}^n \omega_{q_i} - P_{q_1 \ldots q_n}(E)} \tag{2}$$

The damping of n-phonon state is the imaginary part of the analytic continuation in the complex energy plane $E = \omega \pm i\varepsilon$ of the polarization operators $P_{q_1 \ldots q_n}(E)$. It has the form

$$\gamma_{q_1 \ldots q_n}(\omega) = \pi \sum_{n_s > n_{s'}} (n_s - n_{s'}) \sum_{i=1}^n F_{s's}^{(q_i)} \delta(\omega - E_{s'} + E_s - \sum_{j \neq i}^n \omega_{q_j}) \tag{3}$$

The energy of n-phonon state $\bar{\omega}$ is the solution of the equation

$$\bar{\omega} - \sum_{i=1}^n \omega_{q_i} - P_{q_1 \ldots q_n}(\bar{\omega}) = 0. \tag{4}$$

The strength function is calculated as

$$S_{q_1 \ldots q_n}(\omega) = \frac{n!}{\pi} \frac{\gamma_{q_1 \ldots q_n}(\omega)}{(\omega - \bar{\omega})^2 + \gamma_{q_1 \ldots q_n}^2(\omega)}. \tag{5}$$

Putting $q_i = q$ for all i in Eqs. (2) – (5), we obtain the equations for n identical phonon resonance from which we recover the equations for the damping of the GDR, DGDR, and TGDR with $n = 1$, 2, and 3, respectively. The single-particle occupation number n_s (for phonon, ν_q) in Eqs. (2) - (5) has the form of a Fermi (Bose) distribution folded with a distribution of Breit-Wigner type with an ω-dependent width $2\gamma_s(\omega)$ ($2\gamma_q(\omega)$) and centered at: $\tilde{E}_s = E_s + M_s(\tilde{E}_s)$ ($\tilde{\omega}_q = \omega_q + P_q(\tilde{\omega}_q)$). Here M_s and γ_s are mass operator and single-particle damping, respectively [5]. For the ph configurations, the factor $(n_s - n_{s'})$

increases first at low T and decreases at high T. For pp and hh configurations, this factor increases from zero, as T increases, to reach some maximum at T equal to around the shell distance, and decreases at higher T. The region when the maximum is reached corresponds to the observed saturation of the GDR width.

The FWHM $\Gamma_{n\mathrm{GDR}}$ of the n-phonon GDR is determined as

$$\Gamma_{\mathrm{nGDR}} = 2\gamma_{\mathrm{nGDR}}(\bar{\omega}). \tag{6}$$

The integrated yield Y_γ of the γ-ray for the GDR is calculated following the standard statistical model using simplifying assumptions, including a T^2-dependence for the neutron-decay width and the first order of the logarithmic expansion of the level density, namely

$$Y_\gamma \propto \frac{1}{T^2}\int_{E_1}^{E_2} d\omega\omega^3 S_q^{GDR}(\omega)e^{(B_n/T)}/(e^{\omega/T}-1), \quad B_n \text{ is the neutron binding energy.} \tag{7}$$

The effect of angular momentum is included in the PDM via an effective temperature $\tilde{T}$ as follows. The total excitation energy $\tilde{E}^*$ is evaluated as a sum of the Fermi-gas energy $E^* = aT^2$ and the rotational energy $E_{\mathrm{rot}} = J(J+1)/(2\mathcal{J})$ ($\mathcal{J}$ is moment of inertia): $\tilde{E}^* = aT^2 + E_{\mathrm{rot}}$. From the statistical theory of level densities using the Laplace transform, a system with a total excitation energy $\tilde{E}^*$ can be assigned a temperature $\tilde{T}$ according to $\tilde{E}^* = a\tilde{T}^2$. Comparing these two definitions of $\tilde{E}^*$, we find $\tilde{T} = \sqrt{T^2 + J(J+1)/(2a\mathcal{J})}$. This way the results obtained within PDM at an effective temperature $\tilde{T}$ can describe a system at usual temperature T and angular momentum J.

2.2. Energy-weighted sum rule (EWSR) and electromagnetic (EM) cross section of DGDR

The EWSR for DGDR is derived within PDM [7] as $\mathcal{S}_1^{(2)} \simeq 4(\mathcal{S}_1^{(1)} + \frac{1}{2}K)\mathcal{S}_0^{(1)}$, where $K \equiv \langle 0|[D,[V,D]]|0\rangle \simeq 2\sum_{ss'q}\sum_{s_1s_1'} F_{ss'}^{(q)}\langle s_1'|\mathcal{M}(E1)|s'\rangle\langle s|\mathcal{M}(E1)|s_1\rangle\langle 0|a_{s_1}^\dagger a_{s_1'}(Q_q^\dagger + Q_q)|0\rangle$ with $\mathcal{S}_1^{(1)} \equiv \mathrm{TRK} + \rho$ and $\mathcal{S}_0^{(1)}$ being the EWSR and non EWSR of the GDR, respectively. TRK is the Thomas-Reich-Kuhn sum rule, and ρ is the contribution due to exchange forces.

The EM cross section σ_{C} of a relativistic projectile is calculated from the corresponding photoabsorption cross section $\sigma(E)$ and the photon spectral function $N(E)$ as

$$\sigma_{\mathrm{C}}^{(i)} \equiv \int \frac{d\sigma_{\mathrm{C}}}{dE}dE = \int N_i(E)\sigma_i(E)dE, \quad N_i(E) = 2\pi\int_{b_{\min}}^{\infty} \mathrm{e}^{-m(b)}N_i(E,b)bdb, \tag{8}$$

where $N_i(E,b)$ is the virtual photon spectrum from a stationary target seen by a projectile at impact parameter b [10]. The mean number of photons absorbed by the projectile is calculated as $m(b) = \int_{E_{\min}}^{\infty} N_i(E,b)\sigma_i(E)dE$. The photoabsorption cross sections $\sigma_i(E)$ is related to the strength function as $\sigma_i(E) = c^{(i)}S_i(E)E$, where $i = 1$ corresponds to the GDR, $i = 2$ to the DGDR, etc. The GDR strength factor $c^{(1)}$ is defined as

$$c^{(1)} = \frac{(1+\rho)\mathrm{TRK}}{m_1^{(1)}}, \quad m_1^{(1)} = \int_0^{E_{\max}} S_{\mathrm{GDR}}^{\mathrm{PDM}}(E)EdE. \tag{9}$$

The DGDR strength factor $c^{(2)}$ is found as follows. Using (8) and the harmonic limit $S_{\mathrm{DGDR(har)}}^{\mathrm{PDM}}(E)$ of the DGDR strength function, which is obtained by folding two GDR

strength functions within PDM, we write the formal expression of the harmonic limit $\sigma_{\rm C}^{(2)}({\rm har})$ of the EM cross section (8) for DGDR as

$$\sigma_{\rm C}^{(2)}({\rm har}) = \int \frac{d\sigma_{\rm C}^{(2)}}{dE}({\rm har})dE = c^{(2)} \int N_{\rm har}(E) S^{\rm PDM}_{\rm DGDR(har)}(E)E, \quad (10)$$

where $N_{\rm har}(E)$ is calculated using the harmonic limit $\sigma^{PDM}_{\rm DGDR(har)}(E)$ in (8) and $m(b)$. We require this cross section (10) to be equal to the one calculated by folding two GDR cross sections, namely

$$\sigma^{(2)}_{\rm C(f)} \equiv \int \frac{d\sigma^{(2)}_{\rm C(f)}}{dE}dE = \frac{1}{2}\int dE dE_1 dE_2 N(E_1,E_2)\sigma_{\rm GDR}(E_1)\sigma_{\rm GDR}(E_2)\delta(E-E_1-E_2), \quad (11)$$

where $N(E_1, E_2)$ is given in [10]. Equalizing the r.h.s. of (10) and (11), we determine $c^{(2)}$.

3. NUMERICAL RESULTS

3.1. Ingredients of numerical calculations

The Woods - Saxon single-particle energies were used in the calculations of the hot GDR and multiphonon GDRs. The three parameters of the model ω_q, $F^{(q)}_{ph} = F_1$ (for all (ph) states), and $F^{(q)}_{pp'} = F^{(q)}_{hh'} = F_2$ (for all (pp) and (hh) states) are selected as follow. The values of ω_q and F_1 are adjusted at $T = 0$ so that the GDR energy $E_{\rm GDR}$ from Eq. (4) and the GDR width from Eq. (6) ($n = 1$) are equal to their experimental values. The parameter F_2 is chosen so that the GDR energy $E_{\rm GDR}$ remains stable when T varies. This way a unique set of three temperature-independent parameters is determined.

The calculations of EM cross sections of DGDR in ^{136}Xe and ^{208}Pb, and of GDRs in neutron-rich nuclei ^{18,24}O, ^{60}Ca, and ^{150}Sn employ the single-particle energies obtained within the Hartree-Fock (HF) method using the SGII interaction. The GDR strength factor $c^{(1)}$ is found to be 155.314 mb (with $\rho = 0.15$ in (9)) for ^{136}Xe, and 245.408 mb (with $\rho = 0.3$) for ^{208}Pb. The values of $c^{(2)}$ are found to be 42.273 mb for ^{136}Xe, and 97.974 mb for ^{208}Pb. With increasing the number of neutrons, the neutron chemical potential increases sharply and enters the region, where it is surrounded by closely located single-particle levels. The absolute values of the matrix elements $F^{(1)}_{ph}$ for the coupling between the GDR phonon and the ph configurations that correspond to these levels ought to be much larger than those in stable nuclei. In order to simulate this situation, the parameter F_1 has been increased to a value $F_1' \gg F_1$ within the region near the neutron Fermi level $\epsilon^{\rm N}_{\rm F} \geq -8$ MeV, where the difference between the ph-level distance and $|\epsilon_{\rm F}|$ is not larger than a critical distance $\Delta\epsilon_{\rm crit}$. The value $\Delta\epsilon_{\rm crit}$ =1.5 MeV has been used in calculations. The value F_1' has been chosen to obtain the best fit to the experimental running sums of the GDR photoabsorption cross section in ^{18}O. This gives the ratio $F_1' = 40F_1$ that is applied for all nuclei under consideration.

3.2. Results for hot GDR

The solid lines in Fig. 1 are the GDR widths in ^{120}Sn and ^{208}Pb obtained within PDM. A clear saturation of $\Gamma_{\rm GDR}$ is seen at $T \geq 4$ MeV. The GDR width is composed of the quantal width $\Gamma_{\rm Q}$ caused by coupling of GDR phonon to only ph configurations, and the thermal width $\Gamma_{\rm T}$ due to coupling of GDR phonon to only pp and hh configurations at

$T \neq 0$. Γ_Q decreases slowly, while Γ_T increase sharply with increasing T up to $T \simeq 3$ MeV [5,6]. At higher temperatures, Γ_T reaches a saturation. The behavior of the total width Γ_{GDR} at high T is driven mainly by Γ_T.

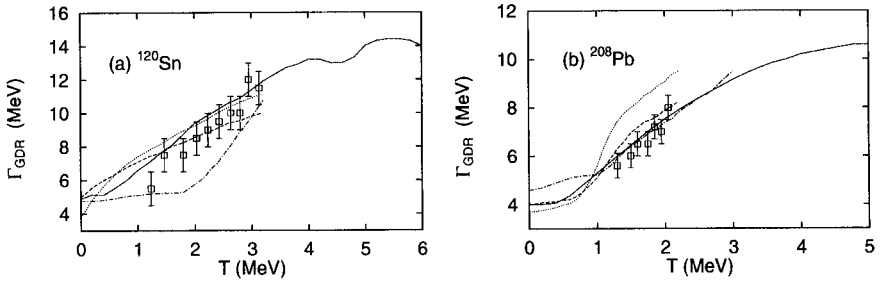

Figure 1. GDR width in ^{120}Sn (a) and ^{208}Pb (b) as a function of temperature T. Solid lines are PDM results; dashed lines: TFM results; dotted: PSM results; dash-dotted lines: CDM results. Inelastic α scattering data are from [1].

Fig. 1 also compares results of PDM with the experimental data [1] and those given by three other models: the thermal fluctuation models (TFM) (dashed), the phenomenological scaling model (PSM) (dotted), and by the collisional damping model (CDM) (dash-dotted) (See [11] and references therein). The TFM gives the values close to those of PDM in both nuclei, although it underestimates the width in ^{120}Sn at $T \geq 3$ MeV. The PSM overestimates strongly the GDR width in ^{208}Pb at $T \geq 1$ MeV. The agreement of the PSM values with the data in ^{120}Sn is obtained using a value of 3.8 MeV for the GDR width at $T = 0$, which is about 1 MeV lower than the experimental one. It is then not clear how the PSM results at $T \neq 0$ will change if the GDR width at $T = 0$ is adjusted to fit the experimental value of around 4.8 MeV. The CDM underestimates the width in ^{120}Sn at T between 1 and 3 MeV. For ^{208}Pb, the widths given by CDM agree well with the data at $T > 1$ MeV, but the value at $T = 0$ is larger than the experimental one by about 0.5 MeV. It is important to notice that all the TFM, PSM, and CDM do not give a width saturation at $T > 3$ MeV while the PDM does.

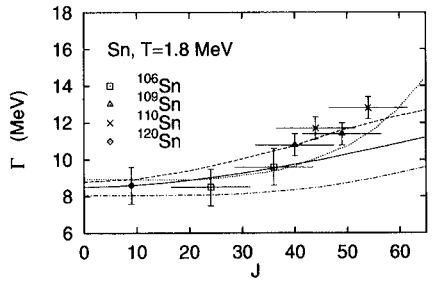

Figure 2. GDR widths as a function of angular momentum J. Results at $T = 1.8$ MeV within PDM are shown as solid line for ^{120}Sn, and dashed line for ^{106}Sn. The corresponding results within TFM are shown as dash-dotted and dotted lines, respectively. Data are from [12].

Shown in Fig. 2 are the GDR widths for ^{106}Sn (solid) and ^{120}Sn (dashed) obtained within PDM at $T = 1.8$ MeV as a function of angular momentum J in comparison with

the experimental data and the prediction of TFM [12]. The angular-momentum effect on the GDR width is stronger in a lighter system (^{106}Sn). For ^{120}Sn, this effect is rather weak up to $J \sim 40\ \hbar$. Compared to the TFM, the PDM gives a stronger increase of width as a function of J up to $J \sim 55\ \hbar$. However, the overall increase of the GDR width with J is still rather weak. At $J \sim 60\ \hbar$, the GDR width in ^{120}Sn increases only by around 1 MeV compared to its value of around 8.5 MeV at $J = 0$. Note that, because the experiments for each isotope were carried out at a fixed excitation energy, the values of temperature at the data point at $J = 36$, 44, and 49 $\hbar$ are significantly different from $T \sim 1.8$ MeV, which is the temperature at which the other points (at J= 24, 40, and 54 $\hbar$) were measured.

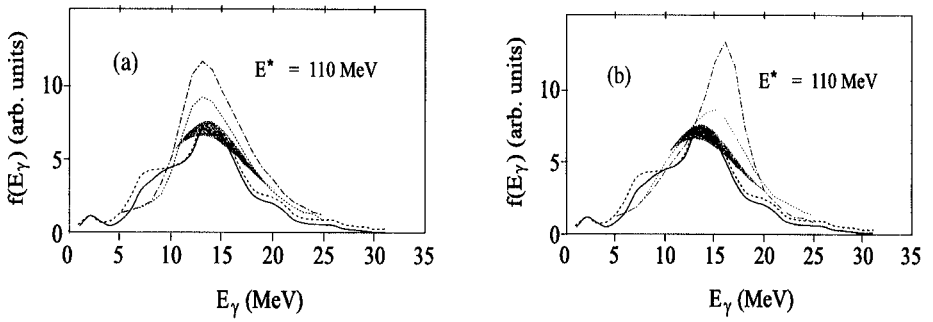

Figure 3. Experimental (shaded area) and theoretical divided spectra of GDR in ^{120}Sn at $E^* = 110$ MeV calculated within CASCADE using the strength functions of PDM (solid: including pairing, dashed: without pairing). Also shown in (a) are results obtained using strength functions of TFM with 100% of EWSR (dash-dotted) and 80% of EWSR (dotted) exhausted, and in (b) are those obtained using strength functions of CDM with free (dotted) and in-medium (dash-dotted) nucleon-nucleon scattering cross section [13].

As the conversion of experimentally measured E^* to T in the models is ambiguous and sometimes misleading [13], we have included the PDM strength functions in the CASCADE calculations to analyze the shape of the hot GDR in ^{120}Sn [14]. The overall GDR shapes at different excitation energies are reproduced reasonably well using the PDM strength functions. An example at $E^* = 110$ MeV is shown in Fig. 3. Inclusion of pairing at $T < 1$ MeV (solid curves) improves significantly the agreement with the data, especially at low E^*. Also shown are results obtained by using the strength functions of TFM and CDM adapted from [13]. Both the TFM and CDM overestimate the GDR shape. At low E^* they underestimate it.

The integrated yields of γ-rays obtained within PDM for hot GDR in ^{120}Sn [6] are shown in Fig. 4 in comparison with the experimental data and predictions by the Milan [8] and Catania [9] models. The PDM reproduces reasonably well the saturation of the yields in both of the GDR region and the region above GDR. The Milan model reproduces the yields only in the GDR region, but strongly overestimates the data in the high-energy region. The Catania model failed to reproduce the data in both regions.

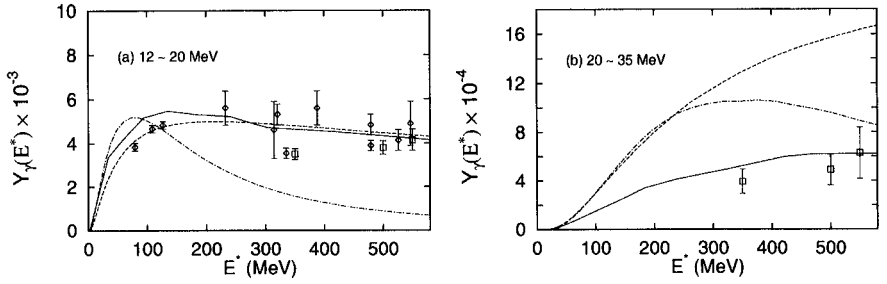

Figure 4. Integrated yields of γ-ray emission for GDR in ^{120}Sn as a function of excitation energy E^* within the GDR region (a) and above the GDR (b). The results of PDM (solid) are compared with those of Milan (dashed) [8], Catania (dash-dotted) [9] models, and the data from RIKEN (diamonds) [3] and MEDEA (boxes) [2] collaborations.

3.3. Results for DGDR and TGDR

Shown in Fig. 5 are the EM differential cross sections of DGDR in ^{136}Xe and ^{208}Pb obtained within the PDM (solid curves) in comparison with the results of folding two Lorentzians (dotted curves), the parameters for each of which fit the experimental values for GDR in these nuclei [15]. The calculated values of the ratio $r \equiv \sigma_C^{\rm DGDR}/\sigma_{C(f)}^{\rm DGDR}$ amount to 1.77 for ^{136}Xe, and 1.40 for ^{208}Pb. They are comparable with the experimentally extracted values, which are 1.78 for ^{136}Xe (on the thin lead target) and 1.33 for ^{208}Pb [4].

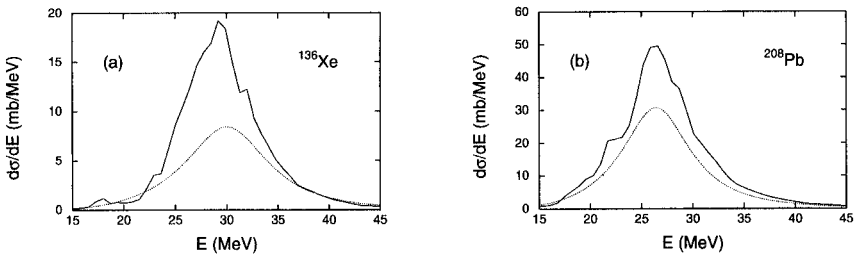

Figure 5. EM differential cross sections for DGDR in ^{136}Xe (a) and ^{208}Pb (b) obtained within PDM (solid lines). The dotted lines are results of folding to Lorentzians for GDRs.

Table 1
Energies E_i, FWHM Γ_i, and EM cross section σ_C^i for GDR (i=GDR) (a) and DGDR (i=DGDR) (b), calculated within PDM (Theory) [15] in comparison with the experimental data (Experiment) [4] for ^{136}Xe and ^{208}Pb

a	E_{GDR} (MeV)		Γ_{GDR} (MeV)		σ_C^{GDR} (mb)	
Nucleus	Theory	Experiment	Theory	Experiment	Theory	Experiment
^{136}Xe	15.6	15.2	4.96	4.8	1676.28	1420(42)±100
^{208}Pb	13.5	13.4	4.04	4.0	3039.67	3280±50
b	E_{DGDR} (MeV)		Γ_{DGDR} (MeV)		σ_C^{DGDR} (mb)	
Nucleus	Theory	Experiment	Theory	Experiment	Theory	Experiment
^{136}Xe	29.2	28.3 ±0.7	7.0	6.3 ±1.6	159.33	164(85)±35
^{208}Pb	26.6	26.6 ±0.8	6.3	6.3 ±1.3	420.92	380 ±40

The peak energies E_i, FWHM Γ_i, and EM cross section σ_C^i for GDR (i=GDR) and DGDR (i=DGDR) calculated within PDM are shown in Table 1 in comparison with the experimental data for ^{136}Xe and ^{208}Pb [4]. As seen in Table 1, all the calculated values are in reasonable agreement with the corresponding experimental data. A systematic comparison between the results for DGDR (index (2) in Fig. 6) and TGDR (index (3)) with anharmonicity and the results obtained by folding two and three GDRs in ^{90}Zr, ^{120}Sn and ^{208}Pb predicts that the TGDR looks more harmonic than the DGDR [7].

3.4. Results for GDR in neutron-rich nuclei

Fig. 7 shows the strength functions of the GDR within PDM for ^{60}Ca at various T [16]. The pigmy resonance is clearly seen below 10 MeV at $T = 0$. It exhausts up to 5% (below 10 MeV) of the EWSR of the GDR (in ^{150}Sn). This pigmy resonance is smoothed out with increasing temperature.

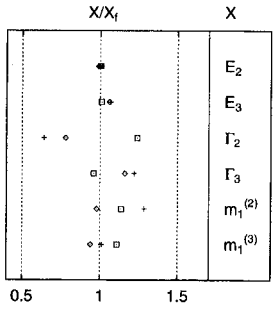

Figure 6. Comparison of quantities X for the DGDR (2) and TGDR (3) with those (X_f) obtained by folding independent GDRs. Diamonds denote results in ^{90}Zr; crosses, results in ^{120}Sn; squares, results in ^{208}Pb.

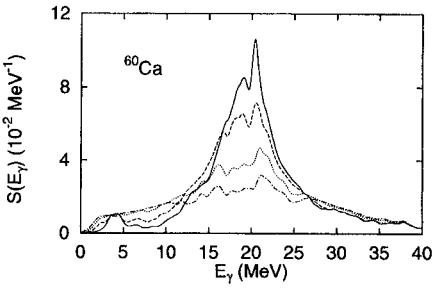

Figure 7. GDR strength functions in ^{60}Ca at $T = 0$ (solid), 1 (dashed), 2 (dotted), and 3 (dash-dotted) MeV.

4. Conclusions

In this work, it has been shown that the PDM is a unified model which has resolved at once the experimental puzzles in the temperature dependence of the hot GDR width and shape, in the EM cross sections of the DGDR in ^{136}Xe and ^{208}Pb, and can be applied to study the pigmy GDR in neutron-rich nuclei. The authentic mechanism that leads to the increase of the GDR width at low T and its saturation at high T within PDM is coupling of GDR phonon to pp and hh configurations at $T \neq 0$. This allows the PDM strength function to be calculated directly in the laboratory frame without any need for an explicit inclusion of thermal fluctuations of shapes. The comparison with predictions given by other existing theories shows that the results of PDM are in best agreement with the experimental data for all of hot GDR characteristics in a wide range of temperatures up to $T \sim 6$ MeV ($E^* \sim 400 - 500$ MeV in tin isotopes). The PDM also shows that it is the first time theory can describe simultaneously the EM cross sections of both GDR and DGDR in both ^{136}Xe and ^{208}Pb. As a future plan, the PDM will be applied to calculate the EM cross sections of pigmy resonances in neutron-rich oxygen isotopes and the results will be compared with the recent experimental data [17].

Thanks are due to A. Ansari, A. Arima, V. Kim Au, K. Eisenman, J. Seitz, T. Suzuki (Nihon university), K. Tanabe, and M. Thoennessen for fruitful collaboration.

REFERENCES

1. T. Baumann et al., Nucl. Phys. A 635 (1998) 428.
2. P. Piattelli et al., Nucl. Phys. A 599 (1996) 63c.
3. K. Yoshida et al., Phys. Lett. B 245 (1990) 7.
4. K. Boretzky et al., Phys. Lett. B 384 (1996) 30; talk at the wokshop on "Double giant resonance", Trento, May 10 - 22, 1999, unpublished
5. N. Dinh Dang and A. Arima, Phys. Rev. Lett. 80 (1998) 4145; Nucl. Phys. A 636 (1998) 443.
6. N. Dinh Dang, K. Tanabe, and A. Arima, Phys. Rev. C 58 (1998) 3374, Nucl. Phys. A 645 (1999) 536.
7. N. Dinh Dang, K. Tanabe, and A. Arima, Nucl. Phys. A 675 (2000) 531.
8. R.A. Broglia, P.F. Bortignon, and A. Bracco, Prog. Part. Nucl. Phys. 28 (1992) 517.
9. A. Bonasera et al., Nucl. Phys. A 569 (1994) 215c.
10. I. A. Pshenichnov et al., Phys. Rev. C 60 (1999) 044901.
11. D. Kusnezov, Y. Alhassid, and K.A. Snover, Phys. Rev. Lett. 81 (1998) 542.
12. A. Bracco et al., Phys. Rev. Lett. 74 (1995) 3748; M. Matiuzzi et al., Nucl. Phys. A 612 (1997) 262.
13. G. Gervais, M. Thoennessen and W.E. Ormand, Phys. Rev. C 58 (1998) R1377.
14. N. Dinh Dang, K. Eisenman, J. Seitz, and M. Thoennessen, Phys. Rev. C 61 (2000) 027302.
15. N. Dinh Dang, V. Kim Au, and A. Arima, preprint RIKEN-AF-NP-349, April 2000.
16. N. Dinh Dang, T. Suzuki, and A. Arima, Phys. Rev. C 61 (2000) 064304.
17. T. Aumann, these proceedings; M. Thoennessen, these proceedings.